

Revealing the Multifunctions of Li_3N in the Suspension Electrolyte for Lithium Metal Batteries

Mun Sek Kim, Zewen Zhang, Jingyang Wang, Solomon T. Oyakhire, Sang Cheol Kim, Zhiao Yu, Yuelang Chen, David T. Boyle, Yusheng Ye, Zhuojun Huang, Wenbo Zhang, Rong Xu, Philaphon Sayavong, Stacey F. Bent, Jian Qin, Zhenan Bao, and Yi Cui*



Cite This: *ACS Nano* 2023, 17, 3168–3180



Read Online

ACCESS |



Metrics & More



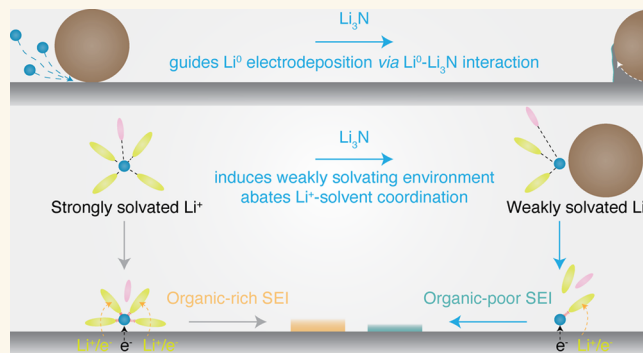
Article Recommendations



Supporting Information

ABSTRACT: Inorganic-rich solid-electrolyte interphases (SEIs) on Li metal anodes improve the electrochemical performance of Li metal batteries (LMBs). Therefore, a fundamental understanding of the roles played by essential inorganic compounds in SEIs is critical to realizing and developing high-performance LMBs. Among the prevalent SEI inorganic compounds observed for Li metal anodes, Li_3N is often found in the SEIs of high-performance LMBs. Herein, we elucidate new features of Li_3N by utilizing a suspension electrolyte design that contributes to the improved electrochemical performance of the Li metal anode. Through empirical and computational studies, we show that Li_3N guides Li electrodeposition along its surface, creates a weakly solvating environment by decreasing Li^+ -solvent coordination, induces organic-poor SEI on the Li metal anode, and facilitates Li^+ transport in the electrolyte. Importantly, recognizing specific roles of SEI inorganics for Li metal anodes can serve as one of the rational guidelines to design and optimize SEIs through electrolyte engineering for LMBs.

KEYWORDS: lithium–metal battery, lithium metal anode, suspension electrolyte, lithium nitride, solid-electrolyte interphase, lithium solvation environment, electrolyte engineering



INTRODUCTION

Reversibly utilizing Li metal (Li^0) anodes is a primary step in successfully developing practical high-energy Li metal batteries (LMBs).^{1,2} Although the Li^0 anode involves a classic electroplating/stripping mechanism, achieving highly reversible and electrochemically stable Li^+ migration at the Li^0 /electrolyte interface becomes challenging due to the inevitable formation of solid-electrolyte interphases (SEIs) on Li^0 anodes with electrolytes.³ Despite the desirable properties of Li^0 anodes, such as a high theoretical specific capacity of 3,861 mAh g^{-1} and a low standard electrode potential of -3.04 V versus standard hydrogen electrodes, the high reactivity of Li^0 makes almost all the possible electrolytes thermodynamically unstable against Li^0 that decompose electrolyte species to form SEIs, in which the properties of SEIs largely influence the electrochemical performance of Li^0 anodes.^{4–6}

During LMB cycles, solvated Li^+ must reversibly migrate across the electrolyte and SEIs on Li^0 anodes, in which characteristics of SEIs predominantly affect Li^+ transport

behavior.³ Essentially, SEIs on Li^0 anodes affect Li^0 electroplating/stripping and Li^+ desolvation processes, thereby dictating the electrochemical performance of Li^0 anodes.^{7–9} Despite the critical functions of SEIs on Li^0 anodes, understanding the roles played by SEI components is still at an early stage to rationally design and manipulate SEIs via electrolyte engineering. As SEI evolutions on Li^0 anodes are directly linked to the solvation structures of Li^+ in electrolytes,³ various modifications to the Li^+ solvation environment and trends have been investigated to correlate SEI properties that positively impact the electrochemical performance of Li^0 anodes. In particular, weakly solvating electrolytes and

Received: December 16, 2022

Accepted: January 23, 2023

Published: January 26, 2023



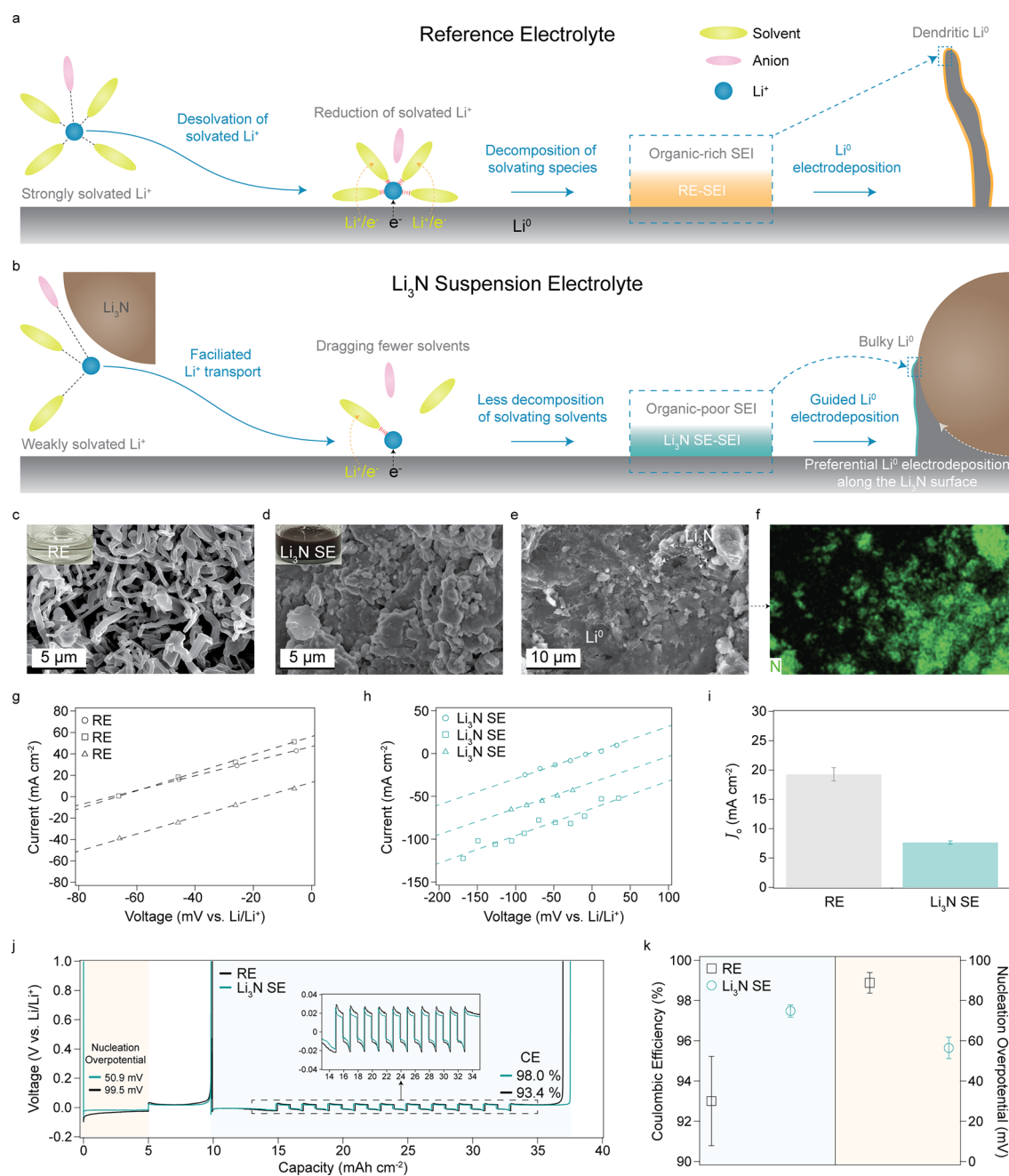


Figure 1. Features of Li_3N for Li^0 anodes. (a) Schematic illustration of strongly solvated Li^+ in RE impacting the SEI evolution on Li^0 anodes and Li^0 electrodeposition. The first step shows Li^+ desolvation and Li^+ reduction processes from the solvated Li^+ in RE. The next step represents the SEI formation on Li^0 anodes by decomposing solvating species that yield organic-rich SEI. The final step delineates the morphology of dendritic Li^0 electrodeposits influenced by RE-SEI. (b) Schematic illustration of weakly solvated Li^+ in Li_3N SE impacting the SEI evolution on Li^0 anodes and Li^0 electrodeposition. The first step represents the weakly solvated Li^+ by Li_3N in the electrolyte, in which fewer solvents are coordinated with Li^+ relative to that in RE. The next step shows facilitated Li^+ transport by the decreased Li^+ -solvent interaction. Then, the weakly solvated Li^+ suppresses decomposition of solvents by dragging relatively fewer solvent molecules close to the Li^0 surface that forms organic-poor SEI. The final step shows bulky Li^0 electrodeposition allowed by the preferential Li^0 deposition across the Li_3N surface and Li_3N SE-SEI. (c) SEM image of Li^0 electrodeposits on Cu from Li/Cu cell with RE at 1 mA cm^{-2} and 1 mAh cm^{-2} . The inset represents the physical image of RE. (d) SEM image of Li^0 electrodeposits on Cu from Li/Cu cell with Li_3N SE at 1 mA cm^{-2} and 1 mAh cm^{-2} . The inset represents the physical image of Li_3N SE (e,f), SEM image (e), and corresponding nitrogen elemental mapping (f) of Li^0 electrodeposits on Cu from Li/Cu cell with exposed Li_3N from Li_3N SE. (g,h) Representative kinetically controlled region from the reverse sweep of ultramicroelectrode cyclic voltammograms for RE (g) and Li_3N SE (h). Three measurements were performed for RE and Li_3N SE. The scan rate and voltage window were 20 V s^{-1} and -1.75 to $2.75 \text{ V vs Li/Li}^+$. (i) Calculated exchange current density (J_0) from g and h for RE ($19.27 \text{ mA cm}^{-2} \pm 1.13 \text{ mA cm}^{-2}$) and Li_3N SE ($7.64 \text{ mA cm}^{-2} \pm 0.28 \text{ mA cm}^{-2}$). (j) Representative voltage profiles of CE measurement from Li/Cu cells with RE and Li_3N SE. The inset represents the zoomed-in voltage profiles from 13 mAh cm^{-2} to 35 mAh cm^{-2} . The background colors represent where the CE and nucleation overpotential were measured. The applied current density was 0.5 mA cm^{-2} . (k) Averaged CE and nucleation overpotential values with standard errors calculated from three identical Li/Cu cells with RE ($93.01\% \pm 2.21\%$ and $88.77 \text{ mV} \pm 5.11 \text{ mV}$) and Li_3N SE ($97.48\% \pm 0.31\%$ and $56.43 \text{ mV} \pm 5.31 \text{ mV}$).

inorganic-rich SEIs were found to be beneficial to the electrochemical performance of Li^0 anodes.^{3,6,10–14}

It has been found that SEIs on Li^0 anodes can swell with electrolytes,¹⁵ indicating that electrolyte species still exist within the SEI domain. This important outcome further justifies the aging of SEIs on Li^0 anodes.¹⁶ In other words, SEIs are still electrolyte penetrable up to a certain degree, and the electrochemical performance of Li^0 anodes are, therefore, affected by both SEIs and the electrolyte species. Furthermore, a modified Li^+ solvation environment by the SEI inorganic compound in the electrolyte has been discovered, which sheds light on the specific features of SEI inorganics that affect SEI evolution and the electrochemical performance of Li^0 anodes.⁶ These combined results suggest that not only can the Li^+ solvation environment within the SEI region be different from the Li^+ solvation environment in the electrolyte, but also the electrochemical performance of SEIs on Li^0 anodes is determined by the distinct SEI inorganic species that sets the specific Li^+ solvation environment within the SEI layer where the actual Li^+ desolvation occurs. These insights lead to a critical hypothesis that the Li^+ solvation shells, not just Li^+ , can migrate across SEIs, in which the solvated Li^+ in the bulk electrolyte further gets modified by the specific inorganic species present in the SEIs on Li^0 anodes. Thus, revealing the roles of inorganic compounds in SEIs is considered one of the fundamental studies to design high-performance SEIs via electrolyte engineering for Li^0 anodes that will potentially lead to the development of advanced electrolytes for developing reliable LMBs.

Among the frequently observed SEI inorganic compounds (e.g., Li_2O , Li_2CO_3 , LiF , Li_3N , Li_2S , ...), Li_3N was particularly found in almost all the high-performance SEIs of Li^0 anodes.³ The beneficial features of Li_3N for Li^0 anodes from prior studies include thermodynamic stability,^{17,18} high Li^+ conductivity,¹⁹ and Li^0 dendrite suppression.^{20–23} Although various forms of Li_3N (pinhole-free film,²³ nanoflowers,²⁴ and nanosheets²⁵) and electrolyte additives (LiN_3 ²⁰ and LiNO_3 ²⁶ to derive Li_3N) have been applied to improve the electrochemical performance of Li^0 anodes, there is still an inadequate understanding of the functional mechanism of Li_3N for Li^0 anodes. Hence, we aim to investigate the further roles of Li_3N in terms of the Li^+ solvation environment and SEI evolution on Li^0 anodes that rationalize the working mechanism of Li_3N for Li^0 anodes and SEIs.

Herein, we designed a Li_3N suspension electrolyte (Li_3N SE) by mixing 80–100 nm Li_3N nanoparticles with a reference electrolyte (RE) of 1 M LiPF_6 in ethylene carbonate (EC) and diethyl carbonate (DEC) (1:1 v/v) with 10 vol % fluoroethylene carbonate (FEC), in which RE serves as one of the most widely studied electrolytes for the SEI analyses of Li^0 anodes.^{6,8,9,15} Also, the electrolyte blend of RE does not contain any nitrogen species that could form Li_3N through the reduction and/or decomposition of RE species, which will help to closely examine the effect of Li_3N in RE. Moreover, utilizing the suspension electrolyte design allows for revealing the functional mechanism of a particular SEI inorganic compound for LMBs.⁶ Thus, Li_3N SE was investigated in detail to identify the Li^+ solvation environment change, SEI evolution on Li^0 anodes, and electrochemical performance. By combining the experimental assessments in tandem with first-principles results, we were able to identify new features of Li_3N in the liquid electrolyte for Li^0 anodes: (i) the surface of Li_3N , especially (001) and (002), is lithiophilic, which guides Li^0

electrodeposition through a favored Li^0 - Li_3N interaction, (ii) Li_3N creates a weakly solvating environment by decreasing Li^+ -solvent interaction in the electrolyte, (iii) Li_3N suppresses solvent decomposition to form organic-poor SEI on Li^0 anodes, and (iv) Li_3N facilitates Li^+ transport in the electrolyte and Li^0 interphase. These findings support the progress of comprehending the improved Li^0 anode performance in connection with the previously reported Li_3N studies and the inorganic-rich SEI concept, particularly having high Li_3N content in the SEIs, of Li^0 anodes. Significantly, beneficial SEI inorganic compounds induce a weakly solvating Li^+ environment by modifying Li^+ -solvent and/or Li^+ -anion coordination,⁶ in which Li_3N is responsible for adjusting Li^+ -solvent coordination, which affects the electrochemical performance of and SEI evolution on Li^0 anodes. Consequently, understanding the unique features of SEI inorganic species can potentially provide scientific and rational guidelines to control and design SEIs on Li^0 anodes by optimizing electrolyte chemistries to improve the electrochemical performance of LMBs.

RESULTS AND DISCUSSION

Analyses of Li_3N in the Electrolyte. Deriving inorganic-rich SEIs by engineering electrolytes became one of the practical approaches to significantly improve the electrochemical performance of Li^0 anodes for LMBs.^{12,13,27,28} Since the SEI evolution on Li^0 anodes is directly associated with the electrolyte,^{3,12,13,28–30} especially its Li^+ solvation environment, understanding the roles played by the major SEI inorganic components, such as Li_2O , Li_2CO_3 , LiF , Li_3N , and Li_2S ,³ can serve as a bridge to connect the mechanism of SEI species and electrochemical performance of Li^0 anodes.⁶ Furthermore, the swelling of SEIs on Li^0 anodes has recently been identified.¹⁵ It has been shown that the degree of SEI swelling correlates to the electrochemical performance of Li^0 anodes, in which inorganic-rich or organic-poor SEIs promote superior electrochemical performance of Li^0 anodes and less SEI swelling.¹⁵ This discovery also leads to an important hypothesis that electrolytes are still present within the SEI layer, where the inorganic compounds in SEIs play an important role in adjusting the Li^+ solvation environment at the interphase of and SEI evolution on Li^0 anodes.⁶ Since Li_3N is a prominent inorganic that exists in the SEIs of many high-performance Li^0 anodes,^{3,20,26,31–39} this study aims to unveil the important roles of Li_3N in terms of Li^+ solvation effects as well as Li^0 electrodeposition stability (Figure 1a,b).

Hypotheses of Li^+ solvation environment, SEI evolution, and Li^0 electrodeposition behavior with RE (Figure 1a) and Li_3N SE (Figure 1b) are illustrated to delineate the features of Li_3N . In Figure 1a, the first step represents the desolvation process of strongly solvated Li^+ by solvents. Then, the solvated Li^+ in RE gets reduced at the surface of Li^0 anodes to form organic-rich SEI. Eventually, the SEI derived from RE (RE-SEI) induces dendritic Li^0 electrodeposition morphology. With Li_3N , the solvated Li^+ becomes weakly solvated relative to that of RE due to the decrease in the Li^+ -solvent interaction by Li_3N in the electrolyte (Figure 1b). Please note that the Li^+ -anion coordination was not affected by the Li_3N in the electrolyte. The weakly solvated Li^+ in Li_3N SE facilitates the transport of solvated Li^+ through the electrolyte and Li^0 interphase. This modified environment of solvated Li^+ in Li_3N SE then suppresses solvent decomposition to form relatively organic-poor SEI on Li^0 anodes. Furthermore, the lithiophilic surface of

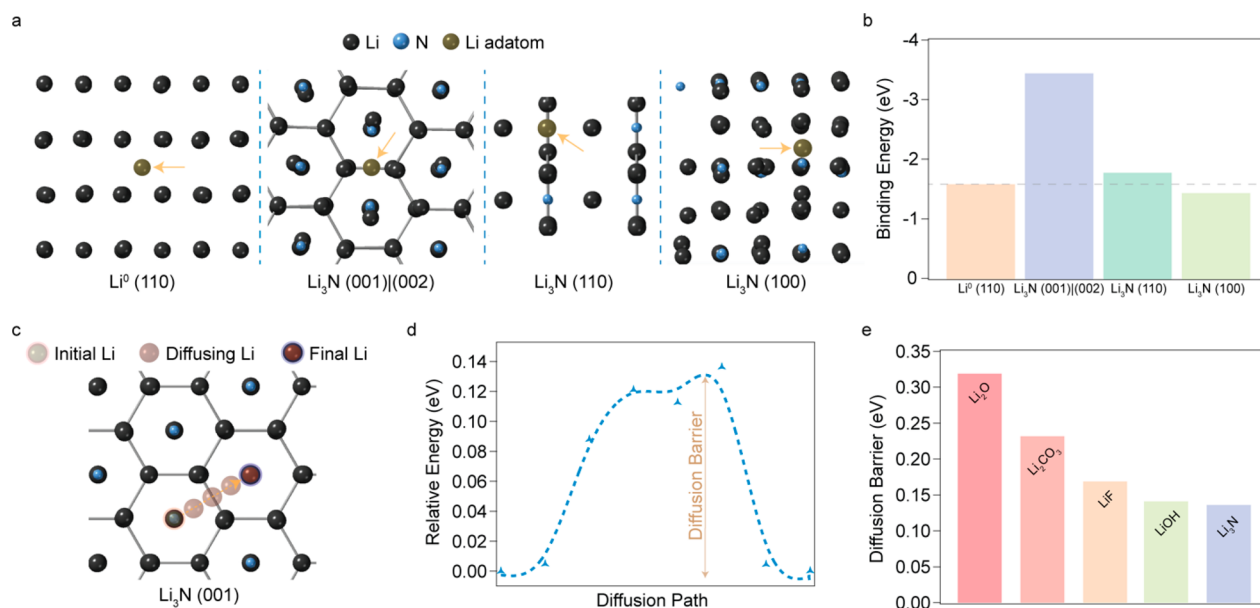


Figure 2. DFT analyses of Li₃N. (a) Li adatom binding sites of Li⁰ (110) and Li₃N (001)|(002), (110), (100) surfaces. The arrows indicate surface adsorbed Li adatom onto the corresponding surfaces of Li⁰ and Li₃N. The color codes for Li of Li₃N, N, and Li adatom are black, sky-blue, and gray, respectively. (b) Calculated Li adatom binding energies for Li⁰ (110), Li₃N (001)|(002), Li₃N (110), and Li₃N (100) surfaces. The dashed gray line indicates the binding energy of Li⁰ (110). (c) The Li adatom diffusion pathway across Li₃N (001) surface. (d) Relative energies based on the Li adatom diffusion trajectories across Li₃N (001) surface. The diffusion barrier is represented by the magnitude between the highest and lowest relative energies. (e) Li adatom surface diffusion barriers for Li₂O (0.319 eV), Li₂CO₃ (0.232 eV), LiF (0.169 eV), LiOH (0.141 eV), and Li₃N (0.133 eV). The diffusion barriers of Li₂O, Li₂CO₃, LiF, and LiOH were retrieved from the literature.⁴⁴

Li₃N and the organic-poor SEI derived from Li₃N SEI (Li₃N SE-SEI) allow bulky Li⁰ electrodeposition. The rest of the discussions are devoted to corroborating these features of Li₃N for Li⁰ anodes.

Observing Li⁰ electrodeposition morphologies became a convenient way to anticipate electrochemical characteristics, such as Coulombic efficiency (CE) and Li nucleation overpotential, of Li⁰ anodes.^{1,40,41} Scanning electron microscopy (SEM) images were examined first to analyze morphological features of Li⁰ electrodeposits with RE and Li₃N SE (Figure 1c–f). High surface area and dendritic Li⁰ morphologies were observed with RE (Figure 1c). On the other hand, the Li⁰ electrodeposits with Li₃N SE exhibited nondendritic morphology (Figure 1d). Notably, Li₃N in Li₃N SE were embedded into the Li⁰ electrodeposits, alluding to preferential Li⁰ electrodeposition along the surfaces of Li₃N (Figure 1d,e). The elemental mapping of nitrogen shown in Figure 1e via energy-dispersive X-ray spectroscopy (EDXS) confirmed that the observed particles were Li₃N as Li₃N was the only nitrogen-containing species in Li₃N SE (Figure 1f). To justify the guided Li⁰ electrodeposition toward Li₃N, the low-magnification SEM image of the electrodeposited Li⁰ with Li₃N SE is shown in Figure S1a. Figure S1a vividly depicts rough surface features due to the Li₃N network formed by the Li₃N SE, in which the nitrogen mapping indicates that the topmost part is Li₃N (Figure S1b). The carbon and oxygen mapping in Figure S1c,d indirectly illustrate Li⁰ electrodeposits, as they are the major elements for SEIs on Li⁰. Based on Figure S1a–d, the region that exhibits the height variation due to Li₃N was selected and shown in Figure S1e, in which the rough surface region was purposefully chosen to demonstrate the preferred Li⁰ electrodeposition toward Li₃N. Figure S1e evidently shows that Li⁰ was electrodepositing along the surfaces of Li₃N as the bottommost surface was free

of Li dendrites, and the Li₃N was well covered by Li⁰ electrodeposits. Hence, the SEM/EDXS analysis suggest that Li⁰ tends to get electrodeposited along the surfaces of Li₃N.

To electrochemically probe possible Li⁰-Li₃N interactions in Li₃N SE, the exchange current densities (*J*₀) for RE and Li₃N SE were measured with the ultramicroelectrode under a fast scan (20 V s⁻¹) cyclic voltammetry (CV) (Figure 1g–i). The fast scan CV with ultramicroelectrode allows for closely investigating electron transfer kinetics of Li with respect to a particular electrolyte by minimizing the effect of mass transports across electrolytes and SEIs on Li⁰ electrode.⁴² Since *J*₀ reflects the intrinsic rate of electron transfer at the Li⁰/electrolyte interface, any changes in *J*₀ for Li₃N SE would clearly indicate the existence of Li⁰-Li₃N interaction, mainly due to the identical liquid electrolyte used for RE and Li₃N SE. By analyzing the kinetically controlled region⁴² in the voltammograms of RE (Figure 1g) and Li₃N SE (Figure 1h), the averaged *J*₀ for RE and Li₃N SE were calculated as 19.27 mA cm⁻² ± 1.13 mA cm⁻² and 7.64 mA cm⁻² ± 0.28 mA cm⁻², respectively (Figure 1i). The noticeable changes in *J*₀ for Li₃N SE compared to that of RE confirmed the Li⁰-Li₃N interaction, in which the electron transfer was also occurring at the Li⁰/Li₃N interface for Li₃N SE. Also, the Li⁰-Li₃N interaction probed by the *J*₀ supports the lithiophilic feature of Li₃N, which is discussed further in the later section. Moreover, the lower value of *J*₀ for Li₃N SE signifies that the rate of electron transfer with Li₃N SE was slower compared to that with RE. This is obvious due to the additional electron transfer happening at the Li⁰/Li₃N interface that should intrinsically be slower than that at the Li⁰/electrolyte interface. Since Li₃N is a good Li⁺ conductor,¹⁹ the charge transfer occurring at the Li⁰/Li₃N interface further suggests that Li⁰ can be electrodeposited and grow from the surfaces of Li₃N once Li₃N is in contact with Li⁰. In other words, the heterojunction

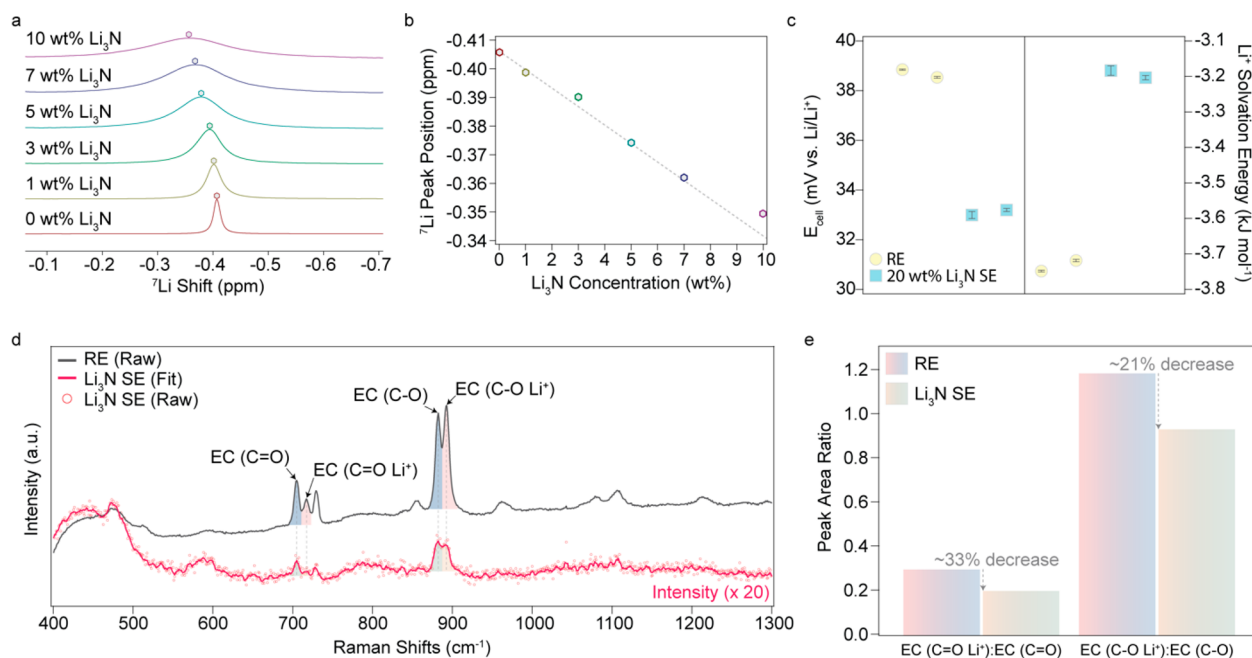


Figure 3. Li^+ solvation environment of Li_3N SE. (a) ^7Li NMR spectrum of 0–10 wt % Li_3N in RE. ^7Li NMR peaks for the corresponding weight content of Li_3N in RE are indicated by the hexagonal symbols. (b) ^7Li NMR peak positions based on 0–10 wt % Li_3N in RE. The dashed gray line represents the linear fit of the peaks. (c) The cell potential (E_{cell}) and Li^+ solvation energy measurements for RE and 20 wt % Li_3N SE. Two measurements were taken for each of the electrolytes. The averaged E_{cell} and solvation energy values with standard errors for RE (1st measurement: 38.850 ± 0.024 mV vs $\text{Li}/\text{Li}^+ | -3.748 \pm -0.002$ kJ mol $^{-1}$ and 2nd measurement: 38.540 ± 0.037 mV vs $\text{Li}/\text{Li}^+ | -3.719 \pm -0.003$ kJ mol $^{-1}$) and 20 wt % Li_3N SE (1st measurement: 32.992 ± 0.139 mV vs $\text{Li}/\text{Li}^+ | -3.183 \pm -0.013$ kJ mol $^{-1}$ and 2nd measurement: 33.197 ± 0.061 mV vs $\text{Li}/\text{Li}^+ | -3.203 \pm -0.006$ kJ mol $^{-1}$) were obtained by recording the measurements up to 3 s after the cell potentials were stabilized. (d) Raman spectrum for RE and Li_3N SE. Four major peaks were assigned for EC (C=O), EC (C=O Li^+), EC (C–O), and EC (C–O Li^+). (e) Raman peak area ratios of RE and Li_3N SE for EC (C=O):EC (C=O Li^+) and EC (C–O):EC (C–O Li^+) retrieved from (d).

formed at the $\text{Li}^0/\text{Li}_3\text{N}$ interface can be depicted as the current collector (Li^0 as the electron conductor) and solid electrolyte (Li_3N as the Li^+ conductor) model, in which the charge transfers occurring at the heterojunction allow electro-deposition of Li^0 on the surfaces of Li_3N . Hence, the J_0 measurement substantiates the Li^0 electrodeposition at the $\text{Li}^0/\text{Li}_3\text{N}$ heterojunction (as observed in Figure 1d,e) by electrochemically probing the Li^0 - Li_3N interaction. We note that this outcome was particularly crucial as this serves as the first demonstration that J_0 can also be impacted by the suspension electrolyte design, meaning the J_0 of a particular liquid electrolyte can still be modified without changing the liquid components.

Since lower surface area and more compact Li^0 electro-deposition morphologies indicate high CE and low Li nucleation overpotential,^{1,40,41} CE and Li nucleation overpotential were measured from Li/Cu cells with RE and Li_3N SE to cross-validate the features attained from Figure 1c–f (Figure 1j,k). Figure 1j shows the representative voltage profiles of CE and Li nucleation overpotential measurements for RE and Li_3N SE. From the voltage profile analyses, it is apparent that Li_3N SE exhibited a higher CE and lower Li nucleation barrier than those of RE. Moreover, the inset of Figure 1j showed reduced overpotentials for Li_3N SE, suggesting facilitated Li^+ transport. Duplicate measurements were taken with three identical Li/Cu cells containing each of the electrolytes to calculate averaged CE ($97.48\% \pm 0.31\%$ for Li_3N SE and $93.01\% \pm 2.21\%$ for RE) and Li nucleation overpotentials (56.43 mV ± 5.31 mV for Li_3N SE and 88.77 mV ± 5.11 mV for RE) with standard errors (Figure 1k). Based on the

morphological and electrochemical analyses from Figure 1c–k, three noticeable features of Li_3N were observed: (i) guided Li^0 electrodeposition along the surface of Li_3N , (ii) existence of Li^0 - Li_3N interaction in Li_3N SE, (iii) improved electrochemical performance of Li^0 anodes, and (iv) facilitated Li^+ transport with Li_3N in the liquid electrolyte.

Analyses of Li_3N via First-Principles Calculations. To construe the guided Li^0 electrodeposition along the surfaces of Li_3N (Figure 1d,e), binding energies and diffusion barriers were computed for Li_3N via density functional theory (DFT). Based on X-ray powder diffraction (XRD) of Li_3N , four orientations were found: (001), (100), (002), and (110), of which (001) was the dominant surface of Li_3N (Figure S2). To relatively compare Li adatom binding energies and diffusion barrier of Li_3N , the same analyses were executed with Li^0 (110) as (110) surface is most commonly observed for Li^0 anodes.^{34,43} Figure 2a shows thermodynamically favorable Li adatom binding sites on Li^0 (110), Li_3N (001)|(002), Li_3N (110), and Li_3N (100) surfaces with the corresponding binding energies of -1.59 eV, -3.44 eV, -1.78 eV, and -1.44 eV, respectively (Figure 2b). The Li adatom binding energy trend in Figure 2b suggests that Li_3N (001)|(002) surfaces (please note that the (002) surface is equivalent to the (001) surface of Li_3N) were the most favorable Li adatom binding surfaces. This means that Li thermodynamically prefers to get adsorbed onto Li_3N (001)|(002) surfaces instead of the Li^0 (110) surface. The favored Li adsorption onto Li_3N surfaces further justifies the change in J_0 observed for Li_3N SE (Figure 1i), as the DFT results (Figure 2b) indicate that it is thermodynamically more favorable for Li to

bind with Li_3N rather than with Li^0 . Thereby, the results in Figure 2b rationalize the Li^0 - Li_3N interaction, illustrating favored Li growth at the $\text{Li}^0/\text{Li}_3\text{N}$ heterojunction. Additionally, the binding energies of Li_3N (001)|(002) surfaces were significantly higher, about two folds, than that of Li^0 (110), Li_3N (110), and Li_3N (100) surfaces, in which the binding energies of Li_3N (110) and (100) were comparable to that of Li^0 (110). Since the Li_3N (001) surface was experimentally found to be the primary surface (Figure S2),^{34,43} this supports the claim that Li_3N , specifically Li_3N (001)|(002) surfaces, is lithiophilic, which explains the guided Li^0 electrodeposition along the surfaces of Li_3N .

With the aim of further supporting the stabilized Li^0 electrodeposition with Li_3N , the surface diffusion barrier of Li adatom on the Li_3N (001) surface was calculated as the low diffusion barrier which facilitates surface diffusion of Li to promote uniform Li^0 electrodeposition (Figure 2c).^{43–45} In Figure 2c, Li was diffusing from the nitrogen to the adjacent nitrogen. From this diffusion trajectory, a total of eight relative energies, which represent threshold energies needed to adsorb Li adatom across the diffusion pathway, were computed to figure out the diffusion barrier. The diffusion barrier of Li adatom on Li_3N (001) surface was 0.133 eV (Figure 2d). Then, the diffusion barrier of Li_3N (0.133 eV) was compared with other prominent SEI inorganic compounds, such as Li_2O (0.319 eV), Li_2CO_3 (0.232 eV), LiF (0.169 eV), and LiOH (0.141 eV), to comparatively understand the diffusion barrier for Li_3N .⁴⁴ According to Figure 2e, Li_3N has the lowest diffusion barrier, claiming Li_3N as the most favorable SEI inorganic in terms of Li surface diffusion characteristics. We note that the low diffusion barrier would be an important parameter for ionically conductive inorganics, such as Li_3N , stabilizing the Li^0 electrodeposition at the Li^0 /inorganic heterojunction. Furthermore, the surface energy of Li_3N (001) surface (3.60 meV atom⁻¹ Å⁻²) was higher than that of Li^0 (110) surface (2.58 meV atom⁻¹ Å⁻²), in which the higher surface energy of Li_3N at the $\text{Li}^0/\text{Li}_3\text{N}$ heterojunction suppresses dendritic Li^0 growth (Figure S3).⁴⁶ Hence, the high binding energy, low diffusion barrier, and high surface energy of Li_3N support the observed guided and stabilized Li^0 electrodeposition along the surface of Li_3N observed in Figure 1d,e and Figure S1.

Li^+ Solvation Environment of Li_3N . ^7Li nuclear magnetic resonance (NMR), relative Li^+ solvation energy, and Raman analyses were performed to investigate the Li^+ solvation environment influenced by Li_3N in the electrolyte (Figure 3). Figure 3a shows ^7Li NMR spectra of RE (0 wt % Li_3N) and Li_3N SE (1–10 wt % Li_3N in RE). ^7Li NMR peaks were shifted in the downfield direction, meaning the peaks were moving to the higher parts per million (ppm), as the Li_3N content increased. The peak shifts directly reflect the changes in the Li^+ solvation environment, in which the downfield peak shifts signify decreased electron density around the nuclei of solvated Li^+ in the electrolyte.⁴⁷ As the solid particles in the liquid sample agitate the magnetic field during the NMR measurement, the retrieved signals become heterogeneous, which broadens the ^7Li NMR peak. This means that the peak becomes broader as the suspension concentration increases as shown in Figure 3a. Despite the peak broadening as a function of suspension content, all the peak shapes are symmetric, which confirms that the peak position is shifting with respect to the changes in the suspension content. To verify the ^7Li shift stems from dissociated Li^+ from LiPF_6 , not Li_3N , the ^7Li

NMR spectrum of RE without LiPF_6 , supernatant of Li_3N SE without LiPF_6 , and Li_3N SE without LiPF_6 were measured (Figure S4). The spectra in Figure S4 do not exhibit any peaks, meaning that the dissociated Li^+ from Li_3N was too low to be detected by the ^7Li NMR. Therefore, the ^7Li shift observed in Figure 3a is due to the change in the electron density of dissociated Li^+ nuclei from LiPF_6 , validating that Li_3N is modifying the solvation environment of Li^+ in the suspension electrolyte. The downfield peak shifts observed in Figure 3a illustrate that the solvated Li^+ in Li_3N SE became less coordinated with solvating electrolyte species. Since the peak position varied with respect to the Li_3N contents, the peak positions were plotted in Figure 3b. The peak positions as a function of the Li_3N content were almost linear up to 7 wt %. Then above 7 wt % Li_3N , the peak shift was less in magnitude. Based on the suspension electrolyte design, the dispersity of the suspension also matters to obtain reliable electrochemical performance. Despite the ^7Li downfield peak shift observed for 10 wt % Li_3N in Figure 3b, particle aggregation above 7 wt % was observed (see Figure S4). Since the ^7Li peak shift depends on the surface area to volume ratio⁶ of the Li_3N suspension, Figure 3b correctly shows that the peak shift becomes nonlinear and shifts less above 7 wt %, indicating that the suspension starts to aggregate (reducing the surface area to volume ratio of the suspension) as observed in Figure S5. Hence, 7 wt % Li_3N content was used to analyze the electrochemical performance, as this weight content was the most reliable for making Li_3N SE. Please note that optimizing the suspension content for the suspension electrolytes depends on several parameters (i.e., suspension types, dimensions, geometries, electrolyte formulations, and so on), in which the reported optimized content can be changed when the parameters vary.

To further support the changes in the Li^+ solvation environment of Li_3N , relative Li^+ solvation energies were potentiometrically probed for RE and 20 wt % Li_3N SE. With symmetric Li^0 electrodes and asymmetric electrolytes configured in H-cell, it became possible to electrochemically measure the relative Li^+ solvation energies of electrolytes (Figure 3c).¹¹ The reason for the high weight content of Li_3N used in the Li^+ solvation energy measurement was to vividly observe the direction of the Li^+ solvation energy change for Li_3N SE. From Figure 3c, 20 wt % Li_3N SE exhibited lower cell potential (E_{cell}) and more positive Li^+ solvation energy than those of RE. These results were critical as the lower E_{cell} and higher Li^+ solvation energy cross-check the changes in the Li^+ solvation environment with Li_3N in the electrolyte as observed from ^7Li NMR measurements (Figure 3a).^{6,11} Also, the lower E_{cell} and higher Li^+ solvation energy of 20 wt % Li_3N SE translate to the weakly solvating Li^+ environment.¹¹ This interchangeably means that the interaction between solvated Li^+ and solvating electrolyte species has been weakened by the presence of Li_3N in the electrolyte, which agrees with ^7Li NMR analysis in Figure 3a. Thereby, we concluded that Li_3N in the electrolyte modifies Li^+ solvation environment by decreasing the interaction between Li^+ and solvating electrolyte species, which creates a weakly solvating environment. Also, it is worth mentioning that the weakly solvating environment allows facilitated Li^0 electrodeposition and Li^+ desolvation kinetics, demonstrating beneficial features of Li_3N .⁴²

To verify the decreased interaction between Li^+ and the solvating electrolyte species observed in ^7Li NMR and the relative Li^+ solvation energy analyses in Figure 3a–c, Raman

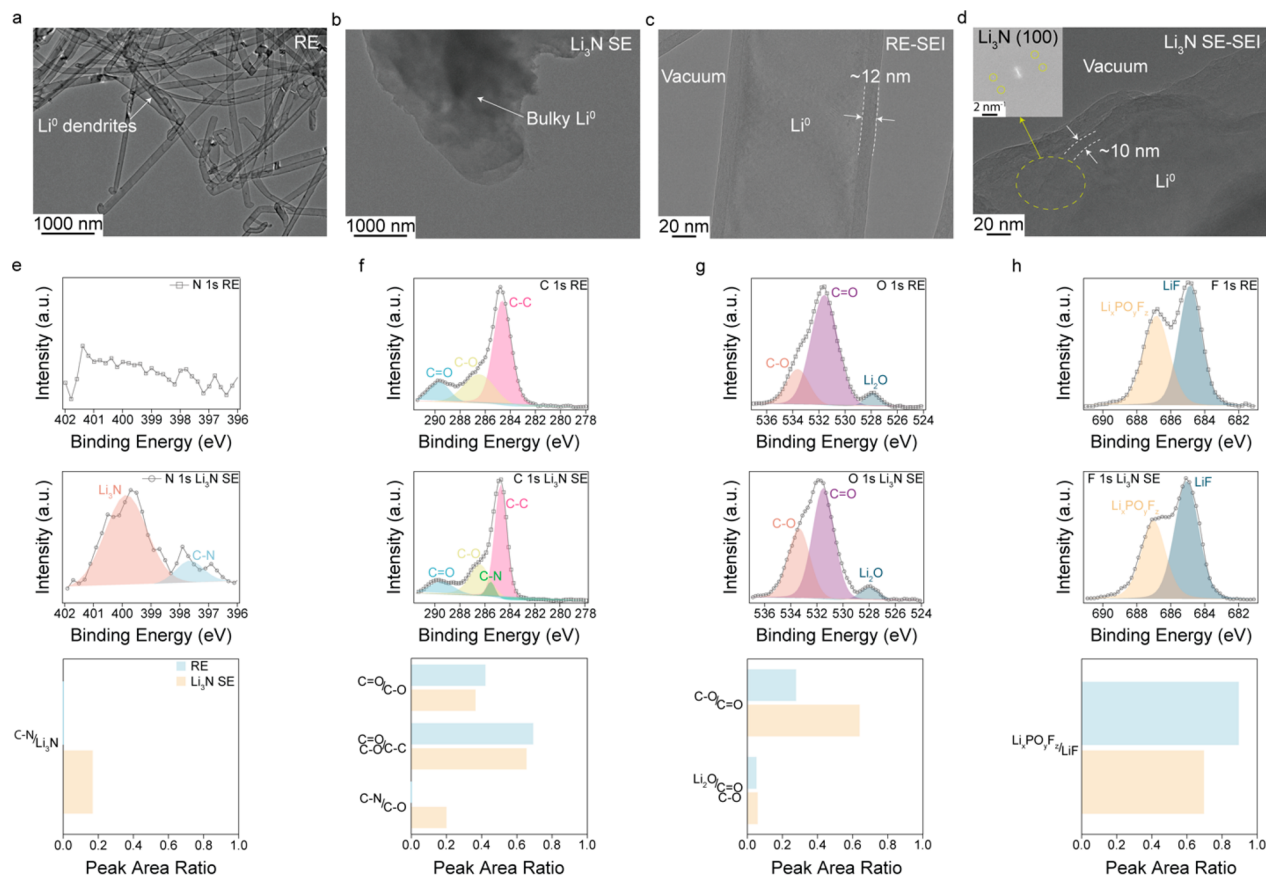


Figure 4. Li^0 interphases with RE and Li_3N SE. (a) A low magnification cryo-TEM image of Li^0 electrodeposits on Cu TEM grid with RE. The arrow indicates dendritic Li^0 electrodeposits with RE. (b) A low magnification cryo-TEM image of Li^0 electrodeposits on Cu TEM grid with Li_3N SE. The arrow indicates bulky Li^0 electrodeposits with Li_3N SE. (c) A high magnification cryo-TEM image of Li^0 dendrite and RE-SEI, indicated by the arrows. (d) A high magnification cryo-TEM image of bulky Li^0 and Li_3N SE-SEI, indicated by the arrows. The inset shows the fast Fourier transform pattern of the image. From the inverse fast Fourier transform of the inset, the dashed yellow circle indicates the position of Li_3N lattice. (e) N 1s XPS spectra of 1 mAh cm^{-2} electrodeposited Li^0 on Cu at 1 mA cm^{-2} from Li/Cu cells with RE and Li_3N SE. The bottom plot represents the peak area ratio of C-N: Li_3N based on N 1s XPS spectra of RE and Li_3N SE. (f) C 1s XPS spectra of 1 mAh cm^{-2} electrodeposited Li^0 on Cu at 1 mA cm^{-2} from Li/Cu cells with RE and Li_3N SE. The bottom plot represents the peak area ratio of C=O:C-O, C=O C-O:C-C, and C-N:C-O based on C 1s XPS spectra of RE and Li_3N SE. (g) O 1s XPS spectra of 1 mAh cm^{-2} electrodeposited Li^0 on Cu at 1 mA cm^{-2} from Li/Cu cells with RE and Li_3N SE. The bottom plot represents the peak area ratio of C-O:C=O and Li_2O :C=O C-O based on O 1s XPS spectra of RE and Li_3N SE. (h) F 1s XPS spectra of 1 mAh cm^{-2} electrodeposited Li^0 on Cu at 1 mA cm^{-2} from Li/Cu cells with RE and Li_3N SE. The bottom plot represents the peak area ratio of $\text{Li}_x\text{PO}_y\text{F}_z$:LiF based on F 1s XPS spectra of RE and Li_3N SE.

spectra of RE and Li_3N SE were examined to understand Li^+ to solvent coordination (Figure 3d). Due to the solid nanoparticles in the liquid electrolyte (Li_3N SE), the retrieved intensity for Li_3N SE was relatively lower than that for RE. Despite the low signal, reliable peaks for alkoxy, EC (C-O), and carbonyl, EC (C=O), groups for EC were observed for Li_3N SE (Figure 3d). The peaks around 892 cm^{-1} , 882 cm^{-1} , 718 cm^{-1} , and 705 cm^{-1} represent solvated alkoxy groups of EC with Li^+ , EC (C-O Li^+), nonsolvated alkoxy groups of EC, EC (C-O), solvated carbonyl groups of EC with Li^+ , EC (C=O Li^+), and nonsolvated carbonyl groups of EC, EC (C=O), respectively.^{48,49} To qualitatively compare the Li^+ -EC coordination between RE and Li_3N SE, the corresponding peaks were integrated and normalized to investigate the relative Li^+ -EC coordination, which was denoted as the EC (C=O Li^+):EC (C=O) and EC (C-O Li^+):EC (C-O) ratios. By calculating the peak area ratios in Figure 3e, the decrease in Li^+ -EC coordination was clearly observed for Li_3N SE, in which both EC (C=O Li^+):EC (C=O) and EC (C-O Li^+):EC (C-O) ratios for Li_3N SE showed approximately 33% and 21% relative

decrease compared to those for RE. The decrease in Li^+ -EC coordination for Li_3N SE cross-validates the results from ^7Li NMR (the decrease in electron density around the nuclei of solvated Li^+ in Li_3N SE) and the relative Li^+ solvation energy (weakly solvating Li^+ environment for Li_3N SE) measurements. Thus, these results reveal the essential roles of Li_3N in terms of the Li^+ solvation environment: Li_3N changes Li^+ solvation environment by decreasing the interaction between Li^+ and solvating electrolyte species, and specifically Li_3N weakens the Li^+ -solvent coordination that induces the weakly solvating environment in the electrolyte.

Analyses of Li^0 Interphase. Li^0 electrodeposition morphologies and SEIs with RE and Li_3N SE were investigated via cryogenic transmission electron microscopy (cryo-TEM) to consolidate observed features of Li_3N in Figures 1–3 (Figure 4a–d). With RE, dendritic Li^0 electrodeposition morphology was observed (Figure 4a), as seen in Figure 1c. On the contrary, a bulky Li^0 electrodeposit was observed with Li_3N SE (Figure 4b), indicating a more compact Li^0 electrodeposition with Li_3N in the electrolyte (Figure 1d,e and Figure S1). To

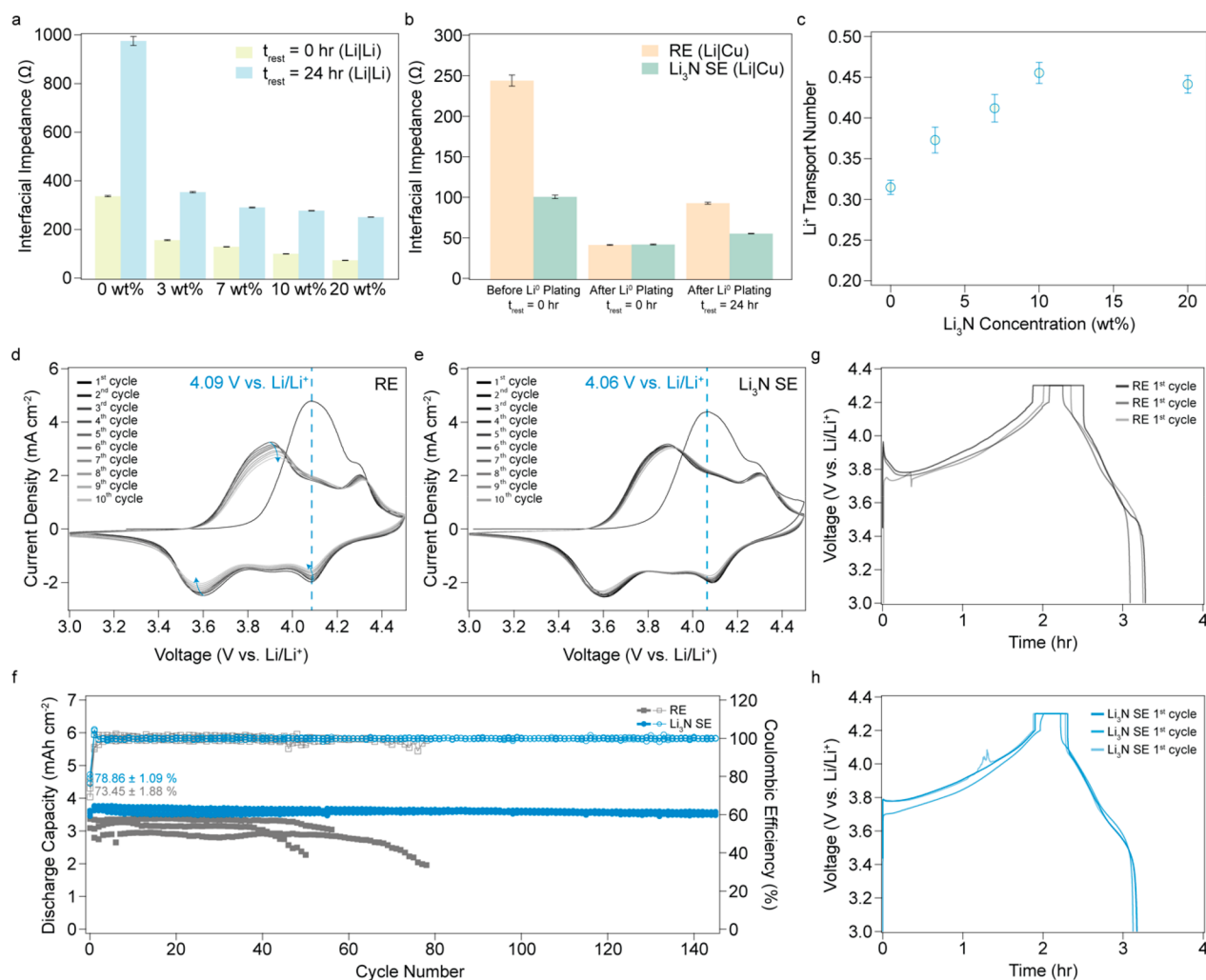


Figure 5. Electrochemical characteristics of Li_3N SE for Li^0 anodes. (a) Measured interfacial impedances from Li|Li cells with 0–20 wt % Li_3N in RE with respect to the aging time ($t_{\text{rest}} = 0$ and 24 h). Three identical Li|Li cells were used for each electrolyte to obtain the averaged interfacial impedances with standard errors. (b) Measured interfacial impedances from Li|Cu cells at $t_{\text{rest}} = 0$ h and after Li^0 electrodeposited on Cu at $t_{\text{rest}} = 0$ and 24 h with RE and Li_3N SE. Three identical Li|Cu cells were used for each condition to obtain the averaged interfacial impedances with standard errors. The current density of 1 mA cm^{-2} and capacity of 1 mAh cm^{-2} were used for plating Li^0 . (c) Li^+ transport number measured from Li|Li cells with 0–20 wt % Li_3N in RE. Three identical Li|Li cells were used for each electrolyte to obtain the averaged Li^+ transport number with standard errors. (d) First 10 cycle cyclic voltammograms of the $\text{Li|Li}_1\text{Ni}_{0.8}\text{Co}_{0.1}\text{Mn}_{0.1}$ cell with RE. The voltage window and scan rate used are 3.0 to 4.5 V vs Li/Li^+ and 0.1 mV s^{-1} . The dashed line indicates the peak position during the first charge cycle of the $\text{Li|Li}_1\text{Ni}_{0.8}\text{Co}_{0.1}\text{Mn}_{0.1}$ cell. The arrows represent the voltage hysteresis during the cell cycling. (e) First 10 cycle cyclic voltammograms of the $\text{Li|Li}_1\text{Ni}_{0.8}\text{Co}_{0.1}\text{Mn}_{0.1}$ cell with Li_3N SE. The voltage window and scan rate used are 3.0 to 4.5 V vs Li/Li^+ and 0.1 mV s^{-1} . The dashed line indicates the peak position during the first charge cycle of the $\text{Li|Li}_1\text{Ni}_{0.8}\text{Co}_{0.1}\text{Mn}_{0.1}$ cell. (f) Cycling profiles of $\text{Li|Li}_1\text{Ni}_{0.8}\text{Co}_{0.1}\text{Mn}_{0.1}$ cells with RE and Li_3N SE. The filled and open symbols represent discharge capacity and CE. The cell cycling was performed using 0.5C charging (0.5C) and 1C discharging (1D) with the voltage window of 3.0–4.3 V vs Li/Li^+ . Three identical Li|NMC811 cells were measured with RE and Li_3N SE, and the averaged first cycle CE with each electrolyte is shown with the standard error. (g) The first cycle voltage profiles of $\text{Li|Li}_1\text{Ni}_{0.8}\text{Co}_{0.1}\text{Mn}_{0.1}$ cells with RE. (h) The first cycle voltage profiles of $\text{Li|Li}_1\text{Ni}_{0.8}\text{Co}_{0.1}\text{Mn}_{0.1}$ cells with Li_3N SE.

look closely into the SEIs on Li^0 with RE (RE-SEI) and Li_3N SE (Li_3N SE-SEI), the thickness of RE-SEI (Figure 4c) and Li_3N SE-SEI (Figure 4d) was estimated with the high magnification cryo-TEM images. The measured SEI thicknesses of RE-SEI and Li_3N SE-SEI were about 12 and 10 nm. Furthermore, the fast Fourier transform (FFT) pattern in the Figure 4d inset exhibits the lattice of Li_3N , indicating the presence of Li_3N in the Li^0 electrodeposits. From the inverse FFT of the Figure 4d inset, the observed Li_3N lattice was mapped in Figure S6 for visualization, in which the detected Li_3N lattice spot is demarcated by a dashed yellow circle in Figure 4d. Therefore, embedded Li_3N into the Li^0 electrodeposit was found for Li_3N SE, in which the presence of

embedded Li_3N in Li^0 electrodeposits further confirmed guided Li^0 electrodeposition behavior along the Li_3N surface as observed in SEM (Figure 1d,e) and DFT (Figure 2) analyses.

X-ray photoelectron spectroscopy (XPS) was performed to analyze chemistries of Li^0 interphases formed by RE and Li_3N SE (Figure 4e–h). Based on N 1s narrow XPS scans, Li_3N and C–N were detected on the Li^0 interphase derived from Li_3N SE, whereas no N 1s signals were retrieved from the Li^0 interphase derived from RE as RE contains no nitrogen species (Figure 4e). The existence of Li_3N can be explained by the guided Li^0 electrodeposition along the surface of Li_3N that gets engulfed during the Li^0 plating (Figure 1d,e, Figure S1, and

Figure 4d). We hypothesize that C–N bonds were formed during the reduction of solvent species at the interface junction between Li_3N and Li^0 , at which the electrolyte should also be reduced at the surface of Li_3N due to the plating potential below 0 V vs Li/Li^+ .³ The ratio of C–N to Li_3N (C–N/ Li_3N) was calculated to understand which species were dominantly present at the Li^0 interphase. The C–N/ Li_3N ratio was around 0.18, indicating that Li_3N more dominantly existed at the Li^0 interphase formed by Li_3N SE (Figure 4e). From C 1s narrow XPS scans (Figure 4f), there were three distinct differences observed between the Li^0 interphase formed by RE and Li_3N SE: (i) a relative increase of C–O, (ii) lower C–C to C–O + C=O ratio (C–C/C–O C=O), and (iii) C–N species for the Li^0 interphase of Li_3N SE. It has been found that enrichment of C–O (alkoxides and ethers) over C=O (carbonates) groups in the organic parts of the SEIs on Li^0 provides improved passivity, enhanced Li^+ transport, and physicochemical stability, implying beneficial features of C–O over C=O species in the SEIs.^{50–53} Also, C=O + C–O over C–C ratio (C–O C=O/C–C) represents a relative solvent decomposition at the interphase of Li^0 anodes, in which C–C and C–O C=O contents should increase and decrease, respectively, upon a more solvent decomposition and complete reduction of solvent molecules to form Li bound species from C–O and C=O groups.^{50–52} The presence of C–N and the low C–N/C–O ratio in Figure 4f also cross-check the observed C–N in Figure 4e. Hence, the lower C=O/C–O and C=O C–O/C–C ratios for Li_3N SE than those for RE suggest a better SEI passivity and a less solvent decomposition on Li^0 anodes. O 1s narrow XPS scans (Figure 4g), which exhibited higher C–O/C=O and $\text{Li}_2\text{O}/\text{C=O}$ C–O ratios for Li_3N SE, showed the same aspects of Li^0 interphase formed by Li_3N SE as observed in Figure 4f. Moreover, a lower $\text{Li}_x\text{PO}_y\text{F}_z/\text{LiF}$ ratio for Li_3N SE than that for RE was observed from F 1s narrow XPS scans (Figure 4h). The lower $\text{Li}_x\text{PO}_y\text{F}_z/\text{LiF}$ ratio for Li_3N SE indicates a reduced solvent decomposition as the oxygen in the $\text{Li}_x\text{PO}_y\text{F}_z$ complex originates from the solvent decomposition with anions. To further verify the reduced solvent decomposition at the Li^0 interphase of Li_3N SE, elemental ratios of P/C, F/C, and O/C were calculated (Figure S7). The lower P/C, F/C, and O/C ratios were achieved for Li_3N SE than those for RE, meaning reduced solvent-derived species for the Li^0 interphase formed by Li_3N SE. Overall, XPS analyses manifest that less solvent decomposition and better Li^0 interphase passivation characteristics were achieved with Li_3N SE. This also confirms the impact of the modified Li^+ solvation environment by Li_3N as observed in Figure 3, in which the decrease in the Li^+ -solvent coordination of solvated Li^+ with Li_3N in the electrolyte suppressed solvent decomposition and promoted a complete solvent decomposition.

Electrochemical Performance Analyses. To understand the electrochemical properties of Li^0 interphase formed by RE and Li_3N SE, interfacial impedances were measured for RE (0 wt % Li_3N) and 3–20 wt % Li_3N SE from LiLi cells before and after aging¹⁶ the cell for a day (Figure 5a, Figure S8, and Table S1). The interfacial impedances of Li^0 with Li_3N SE electrolytes were much lower than that with RE, which can be expected from the weakly solvating environment and organic-poor Li^0 interphase³ with Li_3N . Also, the temporal characteristics of the interfacial impedance changes for Li_3N SE were more stable than that for RE. Moreover, the interfacial stability of electrodeposited Li^0 with RE and Li_3N SE was

investigated by measuring the interfacial impedances before and after Li^0 plating as well as aging the electrodeposited Li^0 for a day from LiCu cells (Figure 5b, Figure S9, and Table S2). The magnitude of the interfacial impedance changes before and after Li^0 plating as well as after aging was lower for Li_3N SE, demonstrating stable electrodeposition of Li^0 with and temporally stabilized Li^0 interphase formed by Li_3N SE. The altered Li^+ solvation environment with Li_3N in the electrolyte contributes to the stabilized temporal characteristics of Li^0 interphase with Li_3N SE, as the decrease in Li^+ -solvent interaction helps to create organic-poor SEI that mitigates SEI swelling.^{3,15} Remarkably, the Li^+ transport number of Li_3N SE increased with the presence of Li_3N in the electrolyte (Figure 5c and Table S3). Having a higher Li^+ transport number can reduce the overpotential, as a larger fraction of the applied current is getting used to migrate Li^+ . To cross-validate the effect of the improved Li^+ transport number, the ionic conductivity was measured for RE ($0.272 \pm 0.008 \text{ mS cm}^{-1}$) and Li_3N SE ($0.261 \pm 0.013 \text{ mS cm}^{-1}$), see Figure S10. The ionic conductivities of RE and Li_3N SE were comparable to each other, indicating that the improved Li^+ transport number with Li_3N SE enables reducing the cell overpotential as the electrolyte conductivity remains similar for RE and Li_3N SE. Accordingly, the decrease in interfacial impedance, increase in Li^+ transport number, and no change in electrolyte ionic conductivity justify the reduced Li^0 -plating/stripping cell overpotential with Li_3N SE, as observed in Figure 1j.

To verify the electrochemical activity of Li_3N in Li_3N SE, cyclic voltammetry scans (from 3 to 4.5 V vs Li/Li^+) and linear sweep voltammetry (LSV, from 3 to 5 V vs Li/Li^+) were performed with $\text{LiLi}_1\text{Ni}_{0.8}\text{Co}_{0.1}\text{Mn}_{0.1}$ and LiAl cells (Figure 5d,e, Figure S11, and Figure S12). By comparing the representative cyclic voltammograms of $\text{LiLi}_1\text{Ni}_{0.8}\text{Co}_{0.1}\text{Mn}_{0.1}$ cells with RE (Figure 5d) and Li_3N SE (Figure 5e), a lower first charging redox potential and less cyclic voltammogram hysteresis,^{43,54} signifying facilitated Li^+ transport and reversible redox reactions in the full cell with Li_3N SE, were observed for Li_3N SE than those for RE. Additional cyclic voltammograms are shown in Figure S11. LSV measurements in Figure S12 revealed that the Li_3N in the electrolyte remains electrochemically stable as no current overshoot was observed. Also, the cyclic voltammograms of LiLiNMC811 with Li_3N SE in Figure 5e did not exhibit additional redox peaks up to 4.5 V vs Li/Li^+ . We hypothesize that oxidizing dispersed Li_3N in the liquid electrolyte may require a higher voltage to oxidize Li_3N as the surfaces of Li_3N are well-wetted by the liquid electrolyte, which can hinder direct contact of dispersed Li_3N with the cathode materials. To confirm the cycling characteristics of $\text{LiLi}_1\text{Ni}_{0.8}\text{Co}_{0.1}\text{Mn}_{0.1}$ full cells with RE and Li_3N SE, cycling and corresponding voltage profiles are illustrated in Figure 5f–h. The full cells with Li_3N SE yielded prolonged cycle life with a higher first cycle CE (Figure 5f). By comparing the first cycle voltage profiles of RE (Figure 5g) and Li_3N SE (Figure 5h) retrieved from Figure 5f, a smaller voltage overshoot at the beginning of the first charging was observed for the Li_3N SE, demonstrating better Li^+ transport and stabilized electrochemical reactions in the full cells.

CONCLUSIONS

By combining empirical and first-principles calculation analyses of Li_3N SE, we showed that Li_3N guides Li^0 electrodeposition along its surface via thermodynamically favored Li^0 - Li_3N interactions, creates the weakly solvating Li^+ environment by

decreasing the interaction between Li^+ and solvating electrolyte species, suppresses solvent decomposition on Li^0 anodes, induces organic-poor SEI on Li^0 anodes, facilitates Li^+ transport in the electrolyte, and promotes reversible electrochemical reactions in the full cells. The outcome of this study can potentially serve as one of the scientific guidelines (i.e., inorganics that promote the weakly solvating Li^+ environment) to rationalize the roles played by inorganic compounds in the SEIs on Li^0 anodes. Importantly, it is crucial to realize that SEIs on Li^0 anodes are still electrolyte permeable, as evidenced by SEI swelling properties,¹⁵ in which solvated Li^+ electrolyte species are present within the SEI layer. Therefore, we must understand how the Li^+ solvation environment is influenced and controlled by SEI inorganic species at the SEI/ Li^0 interface that dictates Li^+ transport as well as charge transfer behavior and impacts SEI evolution on Li^0 anodes. We believe that the systematic revealment of SEI inorganic features would ultimately allow sophisticated electrolyte engineering strategies that contribute to designing high-performance SEIs on Li^0 anodes for realizing reliable yet practical energy-dense LMBs.

METHODS

Materials. The electrolytes were prepared and handled in an Ar-filled glovebox with an O_2 concentration below 0.2 ppm and H_2O concentration below 0.01 ppm. The reference electrolyte (RE) was made with 1 M LiPF_6 in EC:DEC (1:1 v/v) (Gotion LP40) with 10 vol % FEC (Gotion). The Li_3N suspension electrolyte (Li_3N SE) was prepared by mixing indicated amount (3–20 wt %) of Li_3N nanoparticles (80–100 nm in diameter, Nanoshel) with RE. The default weight content of Li_3N for Li_3N SE was 7 wt %, otherwise indicated. High purity Li foil (750 μm thick, 99.9%, Alfa Aesar), Cu foil (Pred Materials), 11 μm thick polyethylene separator (W-Scope), and ~ 4 mAh cm^{-2} NMC811 (Targray) were used to make 2032-type coin cells for Li/Li and Li/Cu, and Li/Li₁Ni_{0.8}Co_{0.1}Mn_{0.1} configured cells.

DFT Calculation. The calculations were performed with the DFT code GPAW.^{55–57} The electron exchange-correlation was described by Perdew–Burke–Ernzerhof functional within the generalized gradient approximation.⁵⁸ The valence electrons are expressed in plane wave basis sets and the core electrons with projector augmented wave (PAW) method. The energy cutoff of 500 eV was applied to all the calculations. The k-point grid of $3 \times 3 \times 1$ was used for all Li_3N -slab calculations, and $5 \times 3 \times 1$ was used for Li slab calculations. The energy and forces per atom were converged to within 10^{-4} eV and 10^{-3} eV/Å, respectively. For the slab calculations, the vacuum of 15 Å thickness is used to reduce periodic artificial interactions. The Li_3N -slab consists of six layers of unit cells (spanning approximately 15 Å) in the z-direction. During geometry optimization, the top 4/5/4/4 layers are allowed to relax for Li (110)/ Li_3N (001)|(002)/ Li_3N (100)/ Li_3N (110) adsorption calculations. The diffusion pathways were calculated via the machine-learning nudged elastic band (ML-NEB) using the CatLearn package,⁵⁹ with nine images between the initial and the final configurations.

XRD. X-ray diffraction (PANalytical Empyrean with a Cu($K\alpha$) X-ray source) was used to examine the crystal structural of Li_3N nanopowder. The Li_3N nanopowders were placed on a glass slide followed by Kapton taping to seal the nanopowders. Then, the diffraction patterns were collected from 10° to 70° using a step size of 0.01.

SEM/EDXS. All the samples were rinsed with pure diethyl carbonate (DEC) and dried inside the Ar glovebox before microscopy. SEM was performed using a Thermo Fisher Scientific Apreo S LoVac Scanning Electron Microscope. Micrographs were taken at a potential of 5 kV and beam current of 50 pA, and the electron signal was collected via the Everhart–Thornley Detector (ETD). Energy dispersive X-ray spectroscopy data was collected with

a Bunker XFlash 6–60 detector at a potential of 10 kV and beam current of 800 pA.

Cryo-TEM. Cu TEM grids were utilized as the working electrode for Li^0 electrodeposition from Li/Cu TEM grid cells. 0.1 mAh cm^{-2} amount of Li was electrodeposited galvanostatically at 1 mA cm^{-2} . After the electrodeposition of Li^0 , the coin cells were disassembled in an argon-filled glovebox. Then, the electrodeposited TEM grids were rinsed with 60 μL of DEC and dried before freezing the sample with liquid nitrogen. After, the sample was instantly submerged in liquid nitrogen to rapidly expose the sample to cryogen without the ambient exposure. For cryo-TEM characterization, while immersed in liquid nitrogen, the sample was loaded into the Gatan side-entry cryotransfer holder (Gatan model 626) and inserted into the TEM column. The cryo-TEM holder uses a specialized cryoshutter to prevent air exposure and ice condensation onto the sample. Once inside the TEM column, the temperature was maintained at approximately -178°C . Cryo-TEM experiments were performed on a Thermo Fisher Titan 80–300 environmental scanning transmission electron microscope operated at an accelerating voltage of 300 kV. The instrument was equipped with an aberration corrector in the image-forming lens, which was tuned before each sample analysis. Cryo-TEM images were acquired by a Gatan K3 IS direct-detection camera in the electron-counting mode. The images were taken with an electron dose rate of around 100 $\text{e}^-/\text{\AA}^2/\text{s}$, a total of 5 frames were taken with 0.1 s per frame for each image.

Li^+ Solvation Energy Measurements. The Li^+ solvation energies of RE and Li_3N SE were probed by Biologic VMP3 using H-cell that contains control electrolyte (1 M LiFSI in DEC)|salt bridge (1 M LiFSI in DME/DOL)|testing electrolytes (RE and 20 wt % Li_3N SE) with submerged Li metal into the control electrolyte and testing electrolytes. The cell potentials and solvation energies for each of the testing electrolytes were recorded for 3 s to obtain averaged values. The detailed apparatus setup can be found in the literature.¹¹

^7Li NMR. An NMR tube with a coaxial insert was used for 1D ^7Li NMR experiments. The outer tube contained freshly prepared RE and (1–10 wt %) Li_3N SE. The inner tube contained deuterated solutions as external references. ^7Li NMR was performed on a Varian Inova 500 MHz NMR spectrometer, and the chemical shifts were referenced to 1 M LiCl in D₂O at 0 ppm.

Raman. Raman spectra were collected with a 532 nm green laser at a Horiba XploRA+ confocal microscope. The electrolytes, RE and Li_3N SE, were sealed in quartz cuvettes under Argon environment.

XPS. The XPS scans were performed on a PHI Versaprobe I with a monochromatized Al $K\alpha$ X-ray source. The XPS chamber was kept at a pressure of about 10^{-7} Pa during the measurements. For the sample preparation, electrodeposited Li^0 on Cu with the capacity and current density of 1 mAh cm^{-2} and 1 mA cm^{-2} was rinsed with 60 μL of DEC in an Ar filled glovebox. A vacuum transfer vessel was used to transfer the samples directly from the Ar glovebox to the vacuum transfer chamber of the instrument to prevent air exposure. High-resolution spectra were calibrated using the C 1s peak at 284.6 eV.

Electrochemical Measurements. The RE (1 M LiPF_6 in EC:DEC (1:1 v/v) with 10 vol % FEC) and Li_3N SE (1–20 wt % Li_3N in RE) were used for the electrochemical measurements. Twenty μL of specified electrolytes were used for Li/Li, Li/Li, Li/Li₁Ni_{0.8}Co_{0.1}Mn_{0.1} cells. The cyclic voltammetry with ultramicroelectrodes for measuring the exchange current density of RE and 20 wt % Li_3N SE was measured by following the literature.⁴² In brief, three electrodes were used: Li metal as the reference/counter electrodes and Cu ultramicroelectrode as the working electrode. The scan rate was 20 V s^{-1} . The voltage window was -1.75 to 2.75 V vs Li/Li⁺. Three measurements were performed to measure averaged exchange current density with statistics. The exchange current density of RE and Li_3N SE was calculated by analyzing the kinetically controlled region in the cyclic voltammograms.⁴² The interfacial impedances were measured by Biologics VMP3 with the frequency ranging from 100 mHz to 7 MHz. For the Li^+ transport number measurements, Li/Li symmetric cells were precycled at 0.5 mA cm^{-2} current density and 1 mAh cm^{-2} areal capacity for 5 cycles. A constant voltage bias of 10 mV was applied for 1 h to obtain initial (I_0) and static (I_s) currents.

The interfacial impedance measurements were carried out before and after the constant voltage step to obtain interfacial resistance before (R_0) and after (R_s). The ionic conductivity of electrolytes was measured by Biologics VMP3 with the frequency ranging from 1 MHz to 100 MHz using symmetric stainless-steel (SS) cells with the 11 μm thick separator (SS/SS cells). The area of 2 cm^2 , distance of 11 μm , and measured solution resistance were used to calculate the ionic conductivity of specified electrolytes. For cycling Li/Cu, Li/Li, and Li/Li₁Ni_{0.8}Co_{0.1}Mn_{0.1} cells, the measurements were recorded by Arbin and Land instruments. For CE and nucleation overpotential measurements with Li/Cu cells, current density of 0.5 mA cm^{-2} was applied with cutoff voltage of 1 V. For cyclic voltammetry, Li/Li₁Ni_{0.8}Co_{0.1}Mn_{0.1} full cells were cycled at 0.1 mV s^{-1} with the voltage window of 3.0 to 4.5 V vs Li/Li⁺ with Biologics VMP3. For the linear sweep voltammetry, the current profiles were obtained from Li/Al cells with RE and Li₃N SE, in which the used voltage window and sweep rate were 3.0–5.0 V vs Li/Li⁺ and 1 mV s^{-1} . For cycling Li/Li₁Ni_{0.8}Co_{0.1}Mn_{0.1} full cells, specified charging and discharge C rates were applied with the voltage window of 3.0–4.3 V, where the constant current goes up to 4.2 V and the constant voltage was held at 4.3 V with the cutoff current value of 0.05 C.

ASSOCIATED CONTENT

Supporting Information

The Supporting Information is available free of charge at <https://pubs.acs.org/doi/10.1021/acsnano.2c12470>.

Morphologies of electrodeposited Li⁰, XRD measurements of Li₃N suspension, surface energies of Li₃N (001) and Li⁰ (110) surfaces, ⁷Li NMR spectra of RE and Li₃N SE without LiPF₆, pictures of 7, 10, and 20 wt % Li₃N SE, overlaid inverse FFT cryo-TEM image of Figure 4d inset, calculated P/C, F/C, and O/C ratios from XPS for electrodeposited Li⁰ with RE and Li₃N SE, Nyquist plots of Li/Li and Li/Cu cells, ionic conductivities of RE and Li₃N SE, cyclic voltammograms of Li/Li₁Ni_{0.8}Co_{0.1}Mn_{0.1} cells with RE and Li₃N SE, linear sweep voltammetry of RE and Li₃N SE, averaged values of the interfacial impedances for Li/Li and Li/Cu cells, and averaged Li⁺ transport numbers (PDF)

AUTHOR INFORMATION

Corresponding Author

Yi Cui – Department of Materials Science and Engineering and Department of Energy Science and Engineering, Stanford University, Stanford, California 94305, United States; Stanford Institute for Materials and Energy Sciences, SLAC National Accelerator Laboratory, Menlo Park, California 94025, United States; orcid.org/0000-0002-6103-6352; Email: yicui@stanford.edu

Authors

Mun Sek Kim – Department of Materials Science and Engineering and Department of Chemical Engineering, Stanford University, Stanford, California 94305, United States

Zewen Zhang – Department of Materials Science and Engineering, Stanford University, Stanford, California 94305, United States; orcid.org/0000-0002-4909-4330

Jingyang Wang – Department of Materials Science and Engineering, Stanford University, Stanford, California 94305, United States; Materials Sciences Division, Lawrence Berkeley Laboratory, Berkeley, California 94720, United States

Solomon T. Oyakhire – Department of Chemical Engineering, Stanford University, Stanford, California 94305, United States; orcid.org/0000-0002-3189-5949

Sang Cheol Kim – Department of Materials Science and Engineering, Stanford University, Stanford, California 94305, United States; orcid.org/0000-0002-1749-8277

Zhiao Yu – Department of Chemical Engineering and Department of Chemistry, Stanford University, Stanford, California 94305, United States; orcid.org/0000-0001-8746-1640

Yuelang Chen – Department of Chemical Engineering and Department of Chemistry, Stanford University, Stanford, California 94305, United States; orcid.org/0000-0002-5249-0596

David T. Boyle – Department of Materials Science and Engineering and Department of Chemistry, Stanford University, Stanford, California 94305, United States; orcid.org/0000-0002-0452-275X

Yusheng Ye – Department of Materials Science and Engineering, Stanford University, Stanford, California 94305, United States; orcid.org/0000-0001-9832-2478

Zhuojun Huang – Department of Materials Science and Engineering and Department of Chemical Engineering, Stanford University, Stanford, California 94305, United States; orcid.org/0000-0001-6236-8693

Wenbo Zhang – Department of Materials Science and Engineering, Stanford University, Stanford, California 94305, United States

Rong Xu – Department of Materials Science and Engineering, Stanford University, Stanford, California 94305, United States; orcid.org/0000-0002-3694-595X

Philaphon Sayavong – Department of Materials Science and Engineering and Department of Chemistry, Stanford University, Stanford, California 94305, United States

Stacey F. Bent – Department of Chemical Engineering, Stanford University, Stanford, California 94305, United States; orcid.org/0000-0002-1084-5336

Jian Qin – Department of Chemical Engineering, Stanford University, Stanford, California 94305, United States; orcid.org/0000-0001-6271-068X

Zhenan Bao – Department of Chemical Engineering, Stanford University, Stanford, California 94305, United States; orcid.org/0000-0002-0972-1715

Complete contact information is available at: <https://pubs.acs.org/doi/10.1021/acsnano.2c12470>

Author Contributions

M.S.K. and Y. Cui conceived the idea and conceptualized the work. M.S.K. performed the experiments and analyzed the data with the guidance from Y. Cui. M.S.K. and Y. Cui wrote the manuscript. Z.Z. performed cryo-TEM analysis. J.W. performed DFT calculations. S.T.O. performed XPS analysis. Z.Y. measured the transport number of the electrolytes. Y. Chen performed ⁷Li NMR of the electrolytes. S.C.K. measured the solvation energy of the electrolytes. D.B. performed transient voltammetry measurements with ultramicroelectrodes. Y.Y. helped electrochemical measurements. Z.H. performed Raman characterization. W.Z. took SEM images. R.X. performed XRD measurements. P.S. provided helpful discussions. S.F.B. reviewed the manuscript. Y. Cui, Z.B., and J.Q. supervised the overall studies. All the authors discussed the manuscript and provided comments.

Notes

The authors declare no competing financial interest.

ACKNOWLEDGMENTS

We acknowledge support from the Assistant Secretary for Energy Efficiency and Renewable Energy, Office of Vehicle Technologies of the US Department of Energy under the Battery Materials Research (BMR) Program and Battery 500 Consortium. Z.Z. acknowledges the support from Stanford Interdisciplinary Graduate Fellowship. S.T.O. acknowledges support from the Knight Hennessy scholarship for graduate studies at Stanford University. J.W. acknowledges computational resources from the Sherlock cluster at Stanford University.

REFERENCES

- (1) Xiao, J.; Li, Q.; Bi, Y.; Cai, M.; Dunn, B.; Glossmann, T.; Liu, J.; Osaka, T.; Sugiura, R.; Wu, B.; Yang, J.; Zhang, J. G.; Whittingham, M. S. Understanding and Applying Coulombic Efficiency in Lithium Metal Batteries. *Nat. Energy*. **2020**, *5*, 561–568.
- (2) Liu, J.; Bao, Z.; Cui, Y.; Dufek, E. J.; Goodenough, J. B.; Khalifah, P.; Li, Q.; Liaw, B. Y.; Liu, P.; Manthiram, A.; Meng, Y. S.; Subramanian, V. R.; Toney, M. F.; Viswanathan, V. v.; Whittingham, M. S.; Xiao, J.; Xu, W.; Yang, J.; Yang, X. Q.; Zhang, J. G. Pathways for Practical High-Energy Long-Cycling Lithium Metal Batteries. *Nat. Energy*. **2019**, *4*, 180–186.
- (3) Wu, H.; Jia, H.; Wang, C.; Zhang, J. G.; Xu, W. Recent Progress in Understanding Solid Electrolyte Interphase on Lithium Metal Anodes. *Adv. Energy Mater.* **2021**, *11*, 2003092.
- (4) Zheng, J.; Kim, M. S.; Tu, Z.; Choudhury, S.; Tang, T.; Archer, L. A. Regulating Electrodeposition Morphology of Lithium: Towards Commercially Relevant Secondary Li Metal Batteries. *Chem. Soc. Rev.* **2020**, *49*, 2701–2750.
- (5) Lin, D.; Liu, Y.; Cui, Y. Reviving the Lithium Metal Anode for High-Energy Batteries. *Nat. Nanotechnol.* **2017**, *12*, 194–206.
- (6) Kim, M. S.; Zhang, Z.; Rudnicki, P. E.; Yu, Z.; Wang, J.; Wang, H.; Oyakhire, S. T.; Chen, Y.; Kim, S. C.; Zhang, W.; Boyle, D. T.; Kong, X.; Xu, R.; Huang, Z.; Huang, W.; Bent, S. F.; Wang, L. W.; Qin, J.; Bao, Z.; Cui, Y. Suspension Electrolyte with Modified Li⁺ Solvation Environment for Lithium Metal Batteries. *Nat. Mater.* **2022**, *21*, 445–454.
- (7) Zachman, M. J.; Tu, Z.; Choudhury, S.; Archer, L. A.; Kourkoutis, L. F. Cryo-STEM Mapping of Solid–Liquid Interfaces and Dendrites in Lithium–Metal Batteries. *Nature*. **2018**, *560*, 345–349.
- (8) Li, Y.; Huang, W.; Li, Y.; Pei, A.; Boyle, D. T.; Cui, Y. Correlating Structure and Function of Battery Interphases at Atomic Resolution Using Cryoelectron Microscopy. *Joule*. **2018**, *2*, 2167–2177.
- (9) Li, Y.; Li, Y.; Pei, A.; Yan, K.; Sun, Y.; Wu, C. L.; Joubert, L. M.; Chin, R.; Koh, A. L.; Yu, Y.; Perrino, J.; Butz, B.; Chu, S.; Cui, Y. Atomic Structure of Sensitive Battery Materials and Interfaces Revealed by Cryo–Electron Microscopy. *Science*. **2017**, *358*, 506–510.
- (10) Wang, H.; Yu, Z.; Kong, X.; Kim, S. C.; Boyle, D. T.; Qin, J.; Bao, Z.; Cui, Y. Liquid Electrolyte: The Nexus of Practical Lithium Metal Batteries. *Joule*. **2022**, *6*, 588–616.
- (11) Kim, S. C.; Kong, X.; Vilá, R. A.; Huang, W.; Chen, Y.; Boyle, D. T.; Yu, Z.; Wang, H.; Bao, Z.; Qin, J.; Cui, Y. Potentiometric Measurement to Probe Solvation Energy and Its Correlation to Lithium Battery Cyclability. *J. Am. Chem. Soc.* **2021**, *143*, 10301–10308.
- (12) Yu, Z.; Wang, H.; Kong, X.; Huang, W.; Tsao, Y.; Mackanic, D. G.; Wang, K.; Wang, X.; Huang, W.; Choudhury, S.; Zheng, Y.; Amanchukwu, C. v.; Hung, S. T.; Ma, Y.; Lomeli, E. G.; Qin, J.; Cui, Y.; Bao, Z. Molecular Design for Electrolyte Solvents Enabling Energy-Dense and Long-Cycling Lithium Metal Batteries. *Nat. Energy*. **2020**, *5*, 526–533.
- (13) Yu, Z.; Rudnicki, P. E.; Zhang, Z.; Huang, Z.; Celik, H.; Oyakhire, S. T.; Chen, Y.; Kong, X.; Kim, S. C.; Xiao, X.; Wang, H.; Zheng, Y.; Kamat, G. A.; Kim, M. S.; Bent, S. F.; Qin, J.; Cui, Y.; Bao, Z. Rational Solvent Molecule Tuning for High-Performance Lithium Metal Battery Electrolytes. *Nat. Energy*. **2022**, *7*, 94–106.
- (14) Hobold, G. M.; Lopez, J.; Guo, R.; Minafra, N.; Banerjee, A.; Shirley Meng, Y.; Shao-Horn, Y.; Gallant, B. M. Moving beyond 99.9% Coulombic Efficiency for Lithium Anodes in Liquid Electrolytes. *Nat. Energy*. **2021**, *6*, 951–960.
- (15) Zhang, Z.; Li, Y.; Xu, R.; Zhou, W.; Li, Y.; Oyakhire, S. T.; Wu, Y.; Xu, J.; Wang, H.; Yu, Z.; Boyle, D. T.; Huang, W.; Ye, Y.; Chen, H.; Wan, J.; Bao, Z.; Chiu, W.; Cui, Y. Capturing the Swelling of Solid-Electrolyte Interphase in Lithium Metal Batteries. *Science*. **2022**, *375*, 66–70.
- (16) Boyle, D. T.; Huang, W.; Wang, H.; Li, Y.; Chen, H.; Yu, Z.; Zhang, W.; Bao, Z.; Cui, Y. Corrosion of Lithium Metal Anodes during Calendar Ageing and Its Microscopic Origins. *Nat. Energy*. **2021**, *6*, 487–494.
- (17) Zhu, Y.; He, X.; Mo, Y. Strategies Based on Nitride Materials Chemistry to Stabilize Li Metal Anode. *Adv. Sci.* **2017**, *4*, 1600517.
- (18) Zhu, Y.; He, X.; Mo, Y. Origin of Outstanding Stability in the Lithium Solid Electrolyte Materials: Insights from Thermodynamic Analyses Based on First-Principles Calculations. *ACS Appl. Mater. Interfaces*. **2015**, *7*, 23685–23693.
- (19) Alpen, U. V. Li₃N: A Promising Li Ionic Conductor. *J. Solid State Chem.* **1979**, *29*, 379–392.
- (20) Eshetu, G. G.; Judez, X.; Li, C.; Bondarchuk, O.; Rodriguez-Martinez, L. M.; Zhang, H.; Armand, M. Lithium Azide as an Electrolyte Additive for All-Solid-State Lithium-Sulfur Batteries. *Angew. Chem., Int. Ed.* **2017**, *56*, 15368–15372.
- (21) Ren, Y.; Yang, S.; Ma, X.; Qi, Z.; Zhang, C.; Liu, X.; Tan, X.; Sun, S. The Li Ion Transport Behavior in the Defect Graphene Composite Li₃N SEI: A First-Principle Calculation. *Mater. Today Chem.* **2021**, *21*, 100510.
- (22) Wang, S.; Chen, J.; Lu, H.; Zhang, Y.; Yang, J.; Nuli, Y.; Wang, J. Artificial Alloy/Li₃N Double-Layer Enabling Stable High-Capacity Lithium Metal Anodes. *ACS Appl. Energy Mater.* **2021**, *4*, 13132–13139.
- (23) Li, Y.; Sun, Y.; Pei, A.; Chen, K.; Vailionis, A.; Li, Y.; Zheng, G.; Sun, J.; Cui, Y. Robust Pinhole-Free Li₃N Solid Electrolyte Grown from Molten Lithium. *ACS Cent. Sci.* **2018**, *4*, 97–104.
- (24) Chen, K.; Pathak, R.; Gurung, A.; Adhamash, E. A.; Bahrami, B.; He, Q.; Qiao, H.; Smirnova, A. L.; Wu, J. J.; Qiao, Q.; Zhou, Y. Flower-Shaped Lithium Nitride as a Protective Layer via Facile Plasma Activation for Stable Lithium Metal Anodes. *Energy Storage Mater.* **2019**, *18*, 389–396.
- (25) Ghosh, A.; Cherepanov, P.; Nguyen, C.; Ghosh, A.; Kumar, A.; Ahuja, A.; Kar, M.; MacFarlane, D. R.; Mitra, S. Simple Route to Lithium Dendrite Prevention for Long Cycle-Life Lithium Metal Batteries. *Appl. Mater. Today*. **2021**, *23*, 101062.
- (26) Piao, N.; Liu, S.; Zhang, B.; Ji, X.; Fan, X.; Wang, L.; Wang, P. F.; Jin, T.; Liou, S. C.; Yang, H.; Jiang, J.; Xu, K.; Schroeder, M. A.; He, X.; Wang, C. Lithium Metal Batteries Enabled by Synergistic Additives in Commercial Carbonate Electrolytes. *ACS Energy Lett.* **2021**, *6*, 1839–1848.
- (27) Yuan, S.; Bao, J. L.; Wang, N.; Zhang, X.; Wang, Y.; Truhlar, D. G.; Xia, Y. Salt-Rich Solid Electrolyte Interphase for Safer High-Energy-Density Li Metal Batteries with Limited Li Excess. *Chem. Commun.* **2020**, *56*, 8257–8260.
- (28) Yamada, Y.; Wang, J.; Ko, S.; Watanabe, E.; Yamada, A. Advances and Issues in Developing Salt-Concentrated Battery Electrolytes. *Nat. Energy*. **2019**, *4*, 269–280.
- (29) Ren, X.; Zou, L.; Cao, X.; Engelhard, M. H.; Liu, W.; Burton, S. D.; Lee, H.; Niu, C.; Matthews, B. E.; Zhu, Z.; Wang, C.; Arey, B. W.; Xiao, J.; Liu, J.; Zhang, J. G.; Xu, W. Enabling High-Voltage Lithium-Metal Batteries under Practical Conditions. *Joule*. **2019**, *3*, 1662–1676.
- (30) Ren, X.; Chen, S.; Lee, H.; Mei, D.; Engelhard, M. H.; Burton, S. D.; Zhao, W.; Zheng, J.; Li, Q.; Ding, M. S.; Schroeder, M.; Alvarado, J.; Xu, K.; Meng, Y. S.; Liu, J.; Zhang, J. G.; Xu, W.

Localized High-Concentration Sulfone Electrolytes for High-Efficiency Lithium-Metal Batteries. *Chem.* **2018**, *4*, 1877–1892.

(31) Fu, L.; Wang, X.; Chen, Z.; Li, Y.; Mao, E.; Seh, Z. W.; Sun, Y. Insights on “Nitrate Salt” in Lithium Anode for Stabilized Solid Electrolyte Interphase. *Carbon Energy* **2022**, *4*, 12–20.

(32) Wen, Y.; Ding, J.; Yang, Y.; Lan, X.; Liu, J.; Hu, R.; Zhu, M. Introducing NO₃⁻ into Carbonate-Based Electrolytes via Covalent Organic Framework to Incubate Stable Interface for Li-Metal Batteries. *Adv. Funct. Mater.* **2022**, *32*, 2109377.

(33) Gu, S.; Zhang, S. W.; Han, J.; Deng, Y.; Luo, C.; Zhou, G.; He, Y.; Wei, G.; Kang, F.; Lv, W.; Yang, Q. H. Nitrate Additives Coordinated with Crown Ether Stabilize Lithium Metal Anodes in Carbonate Electrolyte. *Adv. Funct. Mater.* **2021**, *31*, 2102128.

(34) Ju, Z.; Yuan, H.; Sheng, O.; Liu, T.; Nai, J.; Wang, Y.; Liu, Y.; Tao, X. Cryo-Electron Microscopy for Unveiling the Sensitive Battery Materials. *Small Sci.* **2021**, *1*, 2100055.

(35) Li, Q.; Xue, W.; Peng, J.; Yang, L.; Pan, H.; Yu, X.; Li, H. Synergistic Effect of Temperature and Electrolyte Concentration on Solid-State Interphase for High-Performance Lithium Metal Batteries. *Adv. Energy Sustainability Res.* **2021**, *2*, 2100010.

(36) Liu, D.; Xiong, X.; Liang, Q.; Wu, X.; Fu, H. An Inorganic-Rich SEI Induced by LiNO₃ Additive for a Stable Lithium Metal Anode in Carbonate Electrolyte. *Chem. Commun.* **2021**, *57*, 9232.

(37) Zhang, S.; Yang, G.; Liu, Z.; Li, X.; Wang, X.; Chen, R.; Wu, F.; Wang, Z.; Chen, L. Competitive Solvation Enhanced Stability of Lithium Metal Anode in Dual-Salt Electrolyte. *Nano Lett.* **2021**, *21*, 3310–3317.

(38) Lee, D.; Sun, S.; Kim, C.; Kim, J.; Park, K.; Kwon, J.; Song, D.; Lee, K.; Song, T.; Paik, U. Highly Reversible Cycling with Dendrite-Free Lithium Deposition Enabled by Robust SEI Layer with Low Charge Transfer Activation Energy. *Appl. Surf. Sci.* **2022**, *572*, 151439.

(39) Liu, S.; Ji, X.; Piao, N.; Chen, J.; Eidson, N.; Xu, J.; Wang, P.; Chen, L.; Zhang, J.; Deng, T.; Hou, S.; Jin, T.; Wan, H.; Li, J.; Tu, J.; Wang, C. An Inorganic-Rich Solid Electrolyte Interphase for Advanced Lithium-Metal Batteries in Carbonate Electrolytes. *Angew. Chem., Int. Ed.* **2021**, *60*, 3661–3671.

(40) Adams, B. D.; Zheng, J.; Ren, X.; Xu, W.; Zhang, J. G. Accurate Determination of Coulombic Efficiency for Lithium Metal Anodes and Lithium Metal Batteries. *Adv. Energy Mater.* **2018**, *8*, 1702097.

(41) Pei, A.; Zheng, G.; Shi, F.; Li, Y.; Cui, Y. Nanoscale Nucleation and Growth of Electrodeposited Lithium Metal. *Nano Lett.* **2017**, *17*, 1132–1139.

(42) Boyle, D. T.; Kong, X.; Pei, A.; Rudnicki, P. E.; Shi, F.; Huang, W.; Bao, Z.; Qin, J.; Cui, Y. Transient Voltammetry with Ultramicroelectrodes Reveals the Electron Transfer Kinetics of Lithium Metal Anodes. *ACS Energy Lett.* **2020**, *5*, 701–709.

(43) Kim, M. S.; Deepika; Lee, S. H.; Kim, M.-S.; Ryu, J.-H.; Lee, K.-R.; Archer, L. A.; Cho, W. I. Enabling Reversible Redox Reactions in Electrochemical Cells Using Protected LiAl Intermetallics as Lithium Metal Anodes. *Sci. Adv.* **2019**, *5*, eaax5587.

(44) Cheng, X. B.; Zhao, M. Q.; Chen, C.; Pentecost, A.; Maleski, K.; Mathis, T.; Zhang, X. Q.; Zhang, Q.; Jiang, J.; Gogotsi, Y. Nanodiamonds Suppress the Growth of Lithium Dendrites. *Nat. Commun.* **2017**, *8*, 336.

(45) Lu, Y.; Tu, Z.; Archer, L. A. Stable Lithium Electrodeposition in Liquid and Nanoporous Solid Electrolytes. *Nat. Mater.* **2014**, *13*, 961–969.

(46) Wang, D.; Zhang, W.; Zheng, W.; Cui, X.; Rojo, T.; Zhang, Q. Towards High-Safe Lithium Metal Anodes: Suppressing Lithium Dendrites via Tuning Surface Energy. *Adv. Sci.* **2017**, *4*, 1600168.

(47) Kamphaus, E. P.; Angarita-Gomez, S.; Qin, X.; Shao, M.; Engelhard, M.; Mueller, K. T.; Murugesan, V.; Balbuena, P. B. Role of Inorganic Surface Layer on Solid Electrolyte Interphase Evolution at Li-Metal Anodes. *ACS Appl. Mater. Interfaces.* **2019**, *11*, 31467–31476.

(48) Bouteau, G.; Van-Nhien, A. N.; Sliwa, M.; Sergeant, N.; Lepretre, J. C.; Gachot, G.; Sagaidak, I.; Sauvage, F. Effect of Standard Light Illumination on Electrolyte's Stability of Lithium-Ion Batteries Based on Ethylene and Di-Methyl Carbonates. *Sci. Rep.* **2019**, *9*, 135.

(49) Takekawa, T.; Kamiguchi, K.; Imai, H.; Hatano, M. Physicochemical and Electrochemical Properties of the Organic Solvent Electrolyte with Lithium Bis(Fluorosulfonyl)Imide (LiFSI) As Lithium-Ion Conducting Salt for Lithium-Ion Batteries. *ECS Trans.* **2015**, *64*, 11–16.

(50) Soto, F. A.; Ma, Y.; Martinez De La Hoz, J. M.; Seminario, J. M.; Balbuena, P. B. Formation and Growth Mechanisms of Solid-Electrolyte Interphase Layers in Rechargeable Batteries. *Chem. Matter.* **2015**, *27*, 7990–8000.

(51) Henschel, J.; Peschel, C.; Klein, S.; Horsthemke, F.; Winter, M.; Nowak, S. Clarification of Decomposition Pathways in a State-of-the-Art Lithium Ion Battery Electrolyte through 13 C-Labeling of Electrolyte Components. *Angew. Chem., Int. Ed.* **2020**, *59*, 6128–6137.

(52) Hobold, G. M.; Khurram, A.; Gallant, B. M. Operando Gas Monitoring of Solid Electrolyte Interphase Reactions on Lithium. *Chem. Matter.* **2020**, *32*, 2341–2352.

(53) Saurel, D.; Orayech, B.; Xiao, B.; Carriazo, D.; Li, X.; Rojo, T. From Charge Storage Mechanism to Performance: A Roadmap toward High Specific Energy Sodium-Ion Batteries through Carbon Anode Optimization. *Adv. Energy Mater.* **2018**, *8*, 1703268.

(54) Kim, M. S.; Ryu, J. H.; Deepika; Lim, Y. R.; Nah, I. W.; Lee, K. R.; Archer, L. A.; Cho, W. I. Langmuir–Blodgett Artificial Solid-Electrolyte Interphases for Practical Lithium Metal Batteries. *Nat. Energy.* **2018**, *3*, 889–898.

(55) Mortensen, J. J.; Hansen, L. B.; Jacobsen, K. W. Real-Space Grid Implementation of the Projector Augmented Wave Method. *Phys. Rev. B Condens. Matter Mater. Phys.* **2005**, *71*, 035109.

(56) Enkovaara, J.; Rostgaard, C.; Mortensen, J. J.; Chen, J.; Dulak, M.; Ferrighi, L.; Gavnholt, J.; Glinsvad, C.; Haikola, V.; Hansen, H. A.; Kristoffersen, H. H.; Kuisma, M.; Larsen, A. H.; Lehtovaara, L.; Ljungberg, M.; Lopez-Acevedo, O.; Moses, P. G.; Ojanen, J.; Olsen, T.; Petzold, V.; Romero, N. A.; Stausholm-Møller, J.; Strange, M.; Tritsarlis, G. A.; Vanin, M.; Walter, M.; Hammer, B.; Häkkinen, H.; Madsen, G. K. H.; Nieminen, R. M.; Nørskov, J. K.; Puska, M.; Rantala, T. T.; Schiøtz, J.; Thygesen, K. S.; Jacobsen, K. W. Electronic Structure Calculations with GPAW: A Real-Space Implementation of the Projector Augmented-Wave Method. *J. Phys.: Condens. Matter.* **2010**, *22*, 253202.

(57) Hjorth Larsen, A.; Jørgen Mortensen, J.; Blomqvist, J.; Castelli, I. E.; Christensen, R.; Dulak, M.; Friis, J.; Groves, M. N.; Hammer, B.; Hargus, C.; Hermes, E. D.; Jennings, P. C.; Bjerre Jensen, P.; Kermode, J.; Kitchin, J. R.; Leonhard Kolsbjerg, E.; Kubal, J.; Kaasbjerg, K.; Lysgaard, S.; Bergmann Maronsson, J.; Maxson, T.; Olsen, T.; Pastewka, L.; Peterson, A.; Rostgaard, C.; Schiøtz, J.; Schütt, O.; Strange, M.; Thygesen, K. S.; Vegge, T.; Villhelmsen, L.; Walter, M.; Zeng, Z.; Jacobsen, K. W. The Atomic Simulation Environment - A Python Library for Working with Atoms. *J. Phys.: Condens. Matter.* **2017**, *29*, 273002.

(58) Perdew, J. P.; Burke, K.; Ernzerhof, M. Generalized Gradient Approximation Made Simple. *Phys. Rev. Lett.* **1996**, *77*, 3865.

(59) Garrido Torres, J. A.; Hansen, M. H.; Jennings, P. C.; Boes, J. R.; Bligaard, T. Low-Scaling Algorithm for Nudged Elastic Band Calculations Using a Surrogate Machine Learning Model. *Phys. Rev. Lett.* **2019**, *122*, 156001.